High-Power, High-Speed Velocity-Matched Distributed Photodetectors

L. Y. Lin*, M. C. Wu, and T. Itoh,
UCLA, Electrical Engineering Dept., 405 Hilgard Avenue, Los Angeles, CA 90095-1594
*Current address: AT&T Labs-Research, 791 Holmdel-Keyport Road, Holmdel, NJ 07733

T. A. Vang and R. E. Muller
Jet Propulsion Laboratory, Pasadena, CA 91109

D. L. Sivco and A. Y. Cho
Lucent Technologies Bell Laboratories, Murray Hill, NJ 07974

ABSTRACT

The velocity-matched distributed photodetectors (VMDP) with high saturation power and large bandwidth have been proposed and demonstrated. The theoretical analysis on the trade-off between saturation power and bandwidth shows that VMDP provides fundamental advantages over conventional photodetectors. The theory for designing and simulating the performance of the VMDP is developed comprehensively from the aspect of microwave transmission line, optical waveguide, and the VMDP structure. The VMDP with very high saturation photocurrent (56 mA) and instrument-limited bandwidth (49 GHz) is demonstrated experimentally. The theoretical analysis and experimental results show that VMDP is attractive for high-performance microwave photonics links and high-power optical microwave applications.

Keywords: photodetectors, velocity-matching, saturation power, traveling wave, high-speed.

I. INTRODUCTION

High-power, high-speed photodetectors are the key components for analog fiber-optic links, CATV distribution, and wireless communications with fiber backbone. They are also important for optoelectronic generation of high power microwaves and millimeter-waves and optical heterodyned receivers. Photodetectors with high saturation power can significantly reduce RF insertion loss, increase spurious free dynamic range, and enhance signal-to-noise ratio [1-3]. Significant progress has been achieved for high speed photodetectors using both surface-illuminated [4-6] and waveguide approaches [7,8]. However, the conventional high-speed photodetectors have very small absorption volume (on the order of 1 μm^3) and therefore cannot achieve high saturation power.

Enlarging the effective absorption volume has been proposed as the most direct way to reduce the electric field screening effect caused by the photo-generated carriers under intense illumination. Large core waveguide photodetector has been demonstrated for high saturation power, however, at the expense of its bandwidth because longer detector length is required [9]. Velocity-matched traveling wave photodetectors, first suggested by [10], have been proposed to further increase the absorption volume [11]. However, the difficulty of combining velocity-matched microwave transmission lines with high-speed photodiodes results in very low bandwidth [11].

We propose and demonstrate a *velocity-matched distributed photodetector* (VMDP) to increase the optical saturation power without sacrificing its bandwidth or efficiency. In Sec. II, the principle and physical implementation of the VMDP will be described. Section III presents the theoretical analysis on the trade-off between saturation power and bandwidth for different photodetector approaches. The design issues and the theoretical simulation for the VMDP are elaborated in Sec. IV. In Sec. V, the experimental demonstration of the high-power, high-speed VMDP with nanoscale MSM photodiodes will be reported.

II. THE PROPOSED APPROACH

The schematic drawing of the VMDP is shown in Fig. 1. It consists of an array of small photodiodes serially connected by a passive optical waveguide. The periodic capacitance loading [12] from the photodiodes slows down the microwave velocity to match the velocity of optical wave, as shown in Fig. 2. Because of the dispersion for microwave, there is slight velocity mismatch at high frequency (> 100 GHz). However, compared with the traveling wave photodetector where the microwave transmission line is directly built on top of the waveguide photodetector [8], the velocity mismatch has been greatly reduced.

One unique advantage of the VMDP is that the optical waveguide, photodiodes, and microwave transmission line can be independently optimized. The high-speed performance of the photodetectors is therefore easily retained when designing the velocity-matched 50 Ω transmission line. The traveling-wave property of the VMDP results in a bandwidth essentially limited by that of the individual photodiode, which can be very large since its volume is small. The epitaxial structure of the VMDP is designed such that only fundamental mode exists in both active photodiode and passive waveguide regions and the confinement factor of the wavefunction in the active absorption region is very small to keep the device under saturation. Because of the velocity matching, the photocurrent from each photodiode is summed up *in phase*, and the overall efficiency can still be high [13-15].
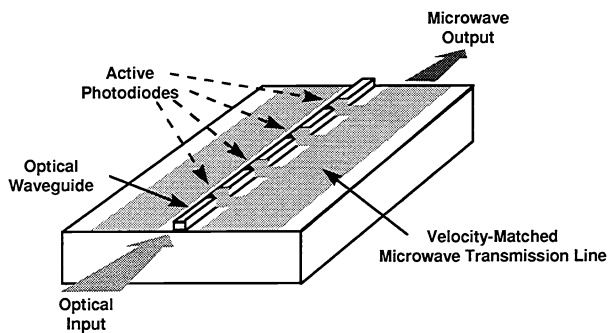
Fig. 1 The schematic drawing of the velocity-matched distributed photodetector (VMDP).
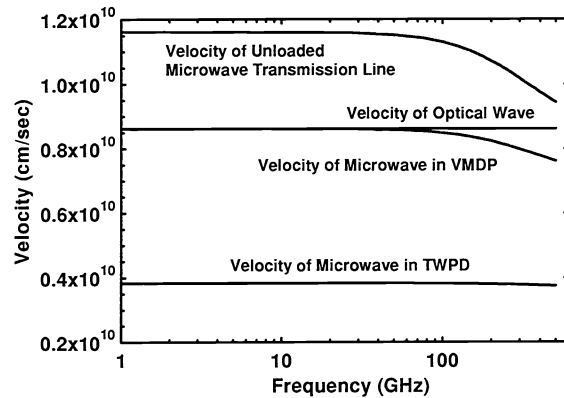
Fig. 2 Velocity matching of optical wave and microwave in VMDP, compared with TWPD (velocity-mismatched).

III. TRADE-OFF BETWEEN SATURATION POWER AND BANDWIDTH

In this section, the theoretical analysis on the trade-off between saturation power and bandwidth for surface-illuminated photodetectors, waveguide photodetectors (WGPD), velocity-mismatched traveling wave photodetectors (TWPD) [8], and the velocity-matched distributed photodetectors (VMDP) will be presented. In contrast to the numerical analysis on the nonlinearities in p-i-n surface-illuminated photodetectors [16], close-form expressions are pursued for the analysis. The 3-dB bandwidth of the surface-illuminated photodetectors and the WGPD is determined by the carrier transit time [17] and the parasitic RC time limitation:

$$f_{3dB} = \left(2.2 \frac{d}{V} + 2\pi \frac{R_L \varepsilon A}{d} \right)^{-1},$$ (1)

where d is the absorption layer thickness, V is the carrier drift velocity (= 8×10^6 cm/sec), A is the detector area (= $W \times L$ for WGPD, W is the waveguide width, and L is the waveguide length), and R_L is the load resistance. In TWPD and VMDP, it is also limited by the velocity mismatch between the optical wave and the generated microwave (the velocity mismatch is minimized in VMDP):

97

$$f_{3dB} = \left(2.2 \frac{d}{V} + 2\pi \frac{R_{TWPD}\varepsilon WL}{d} + 2\pi \cdot L \cdot \frac{V_0 - V_e}{V_o \cdot V_e} \right)^{-1}, \text{ for TWPD} \tag{2}$$

$$f_{3dB} = \left(2.2 \frac{d}{V} + 2\pi \frac{R_{VMDP}\varepsilon W\ell}{d} + 2\pi \cdot (N-1)\Delta \cdot \frac{V_0 - V_e}{V_o \cdot V_e} \right)^{-1}, \text{ for VMDP} \tag{3}$$

where W is the waveguide width, R_{TWPD} and R_{VMDP} are the contact resistance of TWPD and the individual photodiode in VMDP, respectively, L is the length of the TWPD, ℓ is the individual photodiode length for VMDP, Δ is the distance between active photodiodes in VMDP, N is the number of active photodiodes in VMDP, and V_o and V_e are the velocities of optical wave and microwave, respectively. Assuming unity internal quantum efficiency, the saturation photocurrents are expressed as:

$$I_{SAT} = q \int_0^d A \cdot P_0 \cdot \alpha \cdot e^{-\alpha x} dx \tag{4}$$

$$\approx A I_S d, \quad \text{for high - speed operation}$$

for surface-illuminated photodetectors, where α is the absorption coefficient (1/μm), P_o is the incident photon flux (1/μm²/sec), and I_S is the saturation photocurrent density. $I_S = 0.15$ mA/μm³ [16] is employed here for comparing the saturation photocurrent for different photodetectors under the same electric field across the absorption region. The value of I_S can be increased by increasing the applied bias or improving the device design. In Eq. (4), low quantum efficiency ($1 - e^{-\alpha d} \approx \alpha d$) is assumed for high speed surface-illuminated photodetectors [17]. For WGPD, TWPD, and VMDP, the derivations for I_{SAT} result in the same expression:

$$I_{SAT} = \frac{Wd}{\alpha \Gamma} I_S \eta \tag{5}$$

where Γ is the optical confinement factor of the absorption region, and η is the overall quantum efficiency. From Eqs. (1) ~ (5), I_{SAT} can be expressed as a function of d and f_{3dB}. The maximum saturation photocurrent is obtained by optimizing d for the photodetectors, and the results are shown in Fig. 3. The detail of the derivation is reported elsewhere [18]. From Fig. 3, it is found that I_{SAT} is inversely proportional to $f_{3dB}{}^3$. The figure of merit for high-power, high-speed photodetectors can therefore be defined as $I_{SAT} \times f_{3dB}{}^3$, and the results are summarize in Table 1.
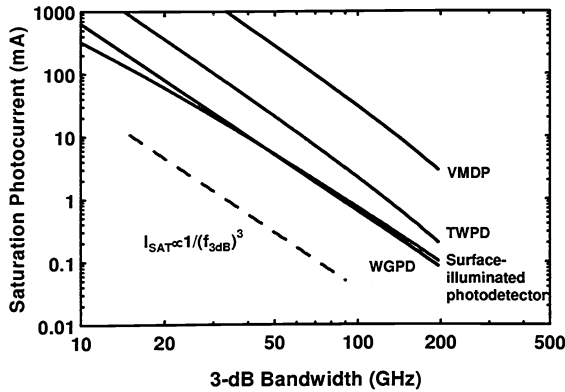
Fig. 3 The trade-off between saturation photocurrent and 3-dB bandwidth for surface-illuminated photodetectors, waveguide photodetectors (WGPD), velocity-mismatched traveling wave photodetectors (TWPD), and velocity-matched distributed photodetectors (VMDP).
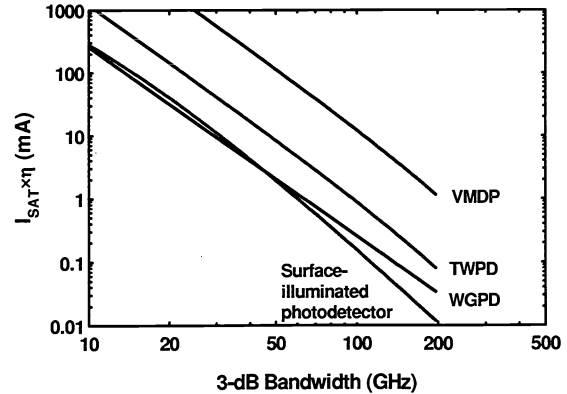
Fig. 4 Saturation photocurrent-quantum efficiency product versus 3-dB bandwidth for surface-illuminated photodetectors, WGPD, TWPD, and VMDP.

98

	Figure of Merit (FOM)
Surface-Illuminated	$I_{SAT} \cdot (f_{3dB})^3 = \dfrac{I_S}{6\pi R_L \varepsilon}\left(\dfrac{V}{3.3}\right)^3 = 8.2 \times 10^5 \ (\mathrm{mA \cdot GHz^3})$
WGPD	$I_{SAT} \cdot (f_{3dB})^3 = \dfrac{I_S}{6\pi R_L \varepsilon}\left(\dfrac{V}{3.3}\right)^3 \dfrac{\eta}{-\ln(1-\eta)} = 6.4 \times 10^5 \ (\mathrm{mA \cdot GHz^3})$
TWPD	$I_{SAT} \cdot (f_{3dB})^3 = \dfrac{I_S}{6\pi R_{TWPD} \varepsilon}\left(\dfrac{V}{3.3}\right)^3 \left(\dfrac{\eta}{-\ln(1-2\eta)}\right)\left(1-\dfrac{f_{3dB}}{f_{vm}}\right)^3$ $= 3.1 \times 10^6 \left(1-\dfrac{f_{3dB}}{f_{vm}}\right)^3 \ (\mathrm{mA \cdot GHz^3})$
VMDP	$I_{SAT} \cdot (f_{3dB})^3 = \dfrac{I_S N}{6\pi R_{VMDP} \varepsilon}\left(\dfrac{V}{3.3}\right)^3 \dfrac{\eta}{-\ln(1-2\eta)} = 4.1 \times 10^7 \ (\mathrm{mA \cdot GHz^3})$

Table 1 Figure of merit (FOM) for high-power, high-speed photodetectors: Surface-illuminated photodetectors, waveguide photodetectors (WGPD), velocity-mismatched traveling wave photodetectors (TWPD), and velocity-matched distributed photodetectors (VMDP).

In Fig. 3, the quantum efficiency is assumed to be 40% for WGPD, TWPD, and VMDP, while it is not fixed for the surface-illuminated photodetectors. For the VMDP, an average 99% velocity matching ($V_o = 8.615 \times 10^9$ cm/sec, $V_e = 0.99 V_o$) is assumed. For TWPD, the velocity of the microwave is equal to 35% of the velocity of the optical wave [8]. The surface-illuminated photodetector and the WGPD have similar performance on the saturation power. However, WGPD can maintain high efficiency when operated in high frequency region [17], as shown in Fig. 4, which shows the saturation photocurrent-quantum efficiency product versus the 3-dB bandwidth. The TWPD has higher saturation power because of the elimination of parasitic resistance loading [8], nevertheless, the saturation power is limited by the velocity mismatch. The VMDP possesses the best performance because of the velocity matching, and long detection length and therefore large saturation photocurrent can be achieved by employing small confinement factor, without sacrificing the bandwidth.

IV. THEORY and DESIGN

IV.1 Equivalent circuit of VMDP

The VMDP is analyzed as a microwave transmission line periodically loaded with active photodiodes, as shown in Fig. 5. The equivalent circuit consists of an array of unit cells comprising a section of transmission line of length Δ, a shunt photodiode admittance Y, and a current source $i_{eff,n}$. The current source $i_{eff,n}$ is related to the photocurrent from individual photodiode $i_{ph,n}$ by

$$i_{eff} = \frac{1}{1+j(\omega/\omega_c)} i_{ph} \tag{6}$$

where $\omega_c = (R_s C_p)^{-1}$ is the RC-limited frequency of the photodiode. The admittance of the photodiode is

$$Y = \frac{1}{R_s + 1/j\omega C_p} \tag{7}$$

The circuit analysis of VMDP is formulated using the transmission matrix method [12]:

$$\begin{bmatrix} V_{n+1} \\ I_{n+1} \end{bmatrix} = \mathbf{M}_2 \cdot \mathbf{M}_1 \cdot \begin{bmatrix} V_n \\ I_n \end{bmatrix} + \begin{bmatrix} 0 \\ i_{eff,n+1} \end{bmatrix} \exp[-j\beta_{opt}(f) \cdot \Delta \cdot n]$$

$$= \mathbf{M}_2 \cdot \mathbf{M}_1 \cdot \begin{bmatrix} V_n \\ I_n \end{bmatrix} + P_{in} \begin{bmatrix} 0 \\ \eta\big((1-\eta)\kappa^2\big)^n \end{bmatrix} \exp[-j\beta_{opt}(f) \cdot \Delta \cdot n] \cdot \frac{1}{1 + j\,\omega/\omega_c} \tag{8}$$

where $\beta_{opt}(f)$ is the phase coefficient of the optical wave, P_{in} is the optical power coupled into the photodetector, η is the internal quantum efficiency of single photodiode, and κ is the field coupling efficiency for the wavefunctions between the active photodiode and the passive waveguide regions. The transmission matrix of the transmission line segment is given by

$$\mathbf{M}_1 = \begin{bmatrix} \cosh(\gamma(f) \cdot \Delta) & \sinh(\gamma(f) \cdot \Delta) \cdot Z(f) \\ \sinh(\gamma(f) \cdot \Delta) \cdot \dfrac{1}{Z(f)} & \cosh(\gamma(f) \cdot \Delta) \end{bmatrix}^{-1}, \tag{9}$$

$$\gamma(f) = \alpha(f) + j \cdot \beta(f), \tag{10}$$

where $Z(f)$ is the characteristic impedance, $\alpha(f)$ and $\beta(f)$ are the total loss and phase coefficient of the microwave transmission line, respectively. The transmission matrix for the photodiode is

$$\mathbf{M}_2 = \begin{bmatrix} 1 & 0 \\ -Y(f) & 1 \end{bmatrix} \tag{11}$$

By applying Eq. (8) recursively, V_N and I_N can be expressed as a function of V_0, I_0, and η. The relations between V_0, I_0 and between V_N, I_N are determined by the terminating impedance of the microwave transmission line. The homogeneous solution of V_N and I_N (denoted as V_N' and I_N') are obtained by setting V_0 and I_0 to zero and applying Eq. (8) iteratively. By superposition principle, the actual V_N and I_N can be derived from

$$\begin{bmatrix} V_N \\ I_N \end{bmatrix} = \begin{bmatrix} V_N' \\ I_N' \end{bmatrix} + (\mathbf{M}_2 \cdot \mathbf{M}_1)^N \mathbf{M}_1^{-1} \cdot \begin{bmatrix} 1 \\ -\dfrac{1}{Z_0} \end{bmatrix} \cdot V_0 \tag{12}$$

In Eq. (12), it is assumed that the transmission line is matched with Z_0 at the input end, as shown in Fig. 5. For the case of open-circuit input termination, the value of Z_0 in Eq. (12) should be set to ∞. The output impedance is matched ($V_N/I_N = Z_0$) in both cases.
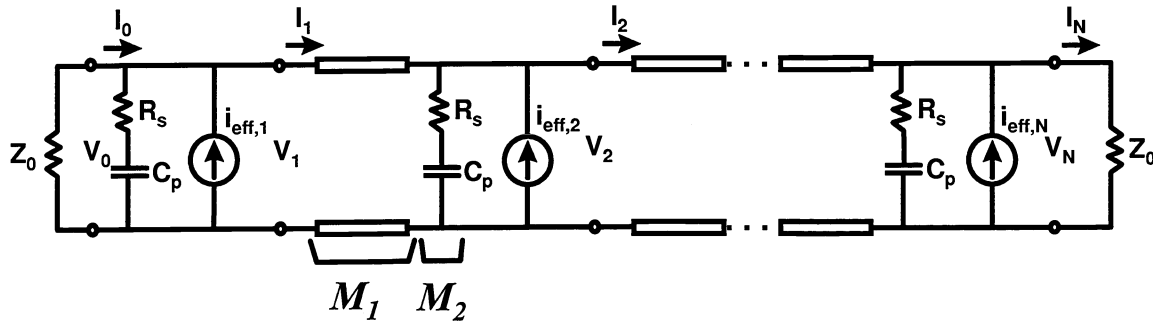
Fig. 5   Equivalent circuit of VMDP.

IV.2 Effect of periodic loading on the microwave transmission line

Coplanar strips (CPS) is employed as the microwave transmission line for VMDP. In the current VMDP design, the CPS has metal line width w equal to 91 μm for both the signal and ground lines. The spacing s between the metal lines is 31 μm. The thickness t of the metal lines is 0.375 μm. The semi-insulating GaAs substrate has a dielectric constant ε_r equal to 12.9 and thickness h equal to 150 μm. For low frequency region where the spacing between the photodiodes is small compared to the wavelength, the effect of periodic loading on the phase velocity of microwave is given by [12]:

100

$$V_L(f) = \left(\sqrt{\left(C_M(f) + \frac{C_P}{\Delta} \right) \cdot L_M(f)} \right)^{-1}, \tag{13}$$

where $C_M(f)$ is the equivalent capacitance [19,20] and $L_M(f)$ is the equivalent inductance per unit length of the transmission line. The impedance of the periodically loaded transmission line can be derived under the same assumption [12]:

$$Z_L(f) = \sqrt{\frac{L_M(f)}{C_M(f) + \frac{C_P}{\Delta}}} \tag{14}$$

In the current VMDP design, metal-semiconductor-metal (MSM) photodiode is chosen as the active photodiode because of its low parasitics and ease of integration with the coplanar microwave transmission line. The parasitic capacitance and resistance of the MSM photodiode can be calculated using the equations in [6]. The current MSM finger pattern has the following geometry: metal line width = 0.3 µm, finger pitch = 0.5 µm, metal thickness = 500 Å, finger length = 18 µm, overlap finger length between electrodes = 7 µm, and the distance between adjacent active photodiodes = 10 × (length of the MSM photodiode). Using these parameters, the phase velocity and the impedance of the periodically-loaded transmission line in VMDP versus the frequency are plotted in Fig. 2 and 6, respectively. Also shown in Fig. 2 is the velocity of optical wave in VMDP obtained from the effective refractive index of the optical waveguide, which will be discussed in Sec. IV.3.
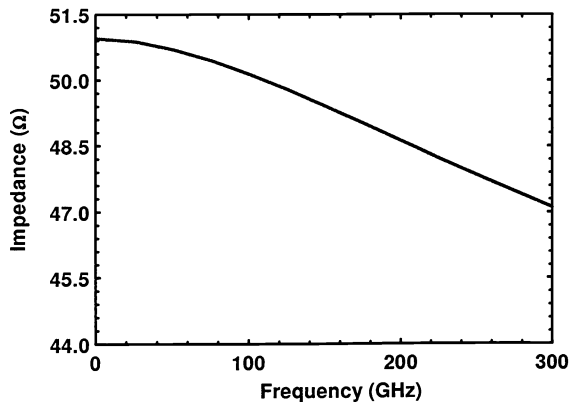
Fig. 6 Impedance of the periodically loaded CPS in VMDP versus the microwave frequency.
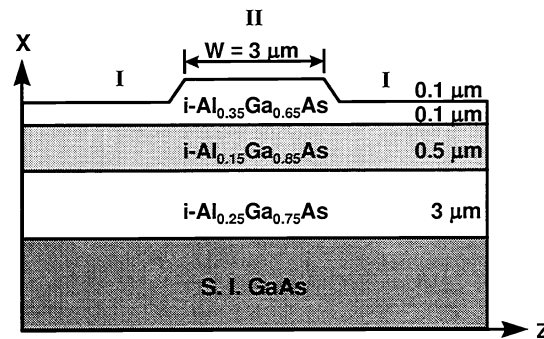
Fig. 7 The layer structure of the ridge waveguide in VMDP.

IV.3 Optical waveguide

The epitaxial layer structure of the device consists of a 3-µm-thick $Al_{0.25}Ga_{0.75}As$ lower cladding layer, a 0.5-µm-thick $Al_{0.15}Ga_{0.85}As$ waveguide core layer, a 0.2-µm-thick $Al_{0.35}Ga_{0.65}As$ upper cladding layer, and a 0.2-µm-thick low-temperature (LT) grown (200°C) GaAs absorbing layer. The absorbing layer is designed to be on the top surface and evanescently coupled to the passive waveguide to facilitate device contact and fabrication. A 3-µm-wide optical ridge waveguide is formed by wet chemical etching of the $Al_{0.35}Ga_{0.65}As$ cladding layer by 0.1 µm depth. To achieve high saturation power, the confinement factor of the MSM absorbing layer is designed to be very low. Furthermore, the structure is designed to have a large circular waveguide mode which results in a more symmetric circular far-field pattern matching that of the optical fiber. High coupling efficiency can therefore be obtained.

The optical effective index of refraction of the ridge waveguide in the VMDP is calculated using the effective index method [21]. The layer structure of the ridge waveguide is shown in Fig. 7. Assuming

101

the optical wavelength equals to 860 nm, there are only fundamental mode solutions for the designed waveguide. The obtained effective indices are: N_I = 3.4809 for the lateral region, N_{II} = 3.4832 and 3.4850+0.00108i for the guided region in the passive optical waveguide and the active photodiode regions, respectively. The effective index in the photodiode region has an imaginary part because of the absorption of optical wave. The effective index N_{eff} for the optical waveguide is 3.4823. The group velocity of the optical wave can therefore be determined using the following equation:

$$V_{opt} = \frac{c}{N_{eff}} = 8.615 \times 10^9 \ (cm/sec) \tag{15}$$

The optical wavefunction in the waveguide can also be decided using the same transfer matrix approach, knowing the effective refractive index N_{II} in the guided region [21]. The real part of the simulated wavefunctions in the passive waveguide and the active photodiode regions are shown in Fig. 8. The coupling efficiency κ is obtained by calculating the overlap integral of the wavefunctions. The theoretical coupling efficiency κ for the VMDP is 97.8%.

The confinement factor Γ is defined by the percentage of the optical field intensity confined in the active absorption GaAs layer. It can be obtained from the optical wavefunction in the active photodiode region:

$$\Gamma = \frac{\int_{x_a}^{x_b} \left| E_y^{active}(x) \right|^2 dx}{\int \left| E_y^{active}(x) \right|^2 dx}, \tag{16}$$

where x_a is the coordinate of $Al_{0.35}Ga_{0.65}As$/GaAs interface, and x_b is the coordinate of GaAs/Air interface. The VMDP has a very low confinement factor (Γ = 1.53%) from the calculation.
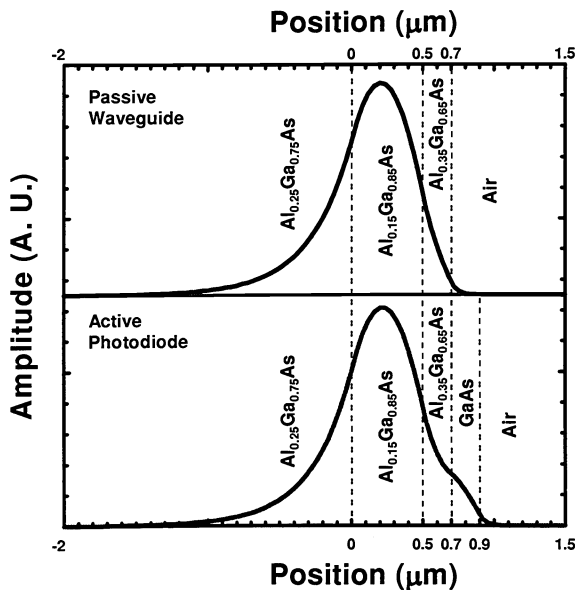
Fig. 8 The optical wavefunctions in the passive waveguide and the active photodiode regions.
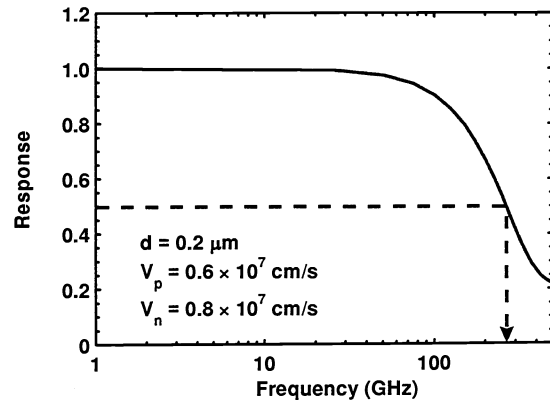
Fig. 9 Transit time frequency response of the MSM photodiode with finger spacing equal to 0.2 μm.

IV.4 Performance of VMDP

The frequency response of the overall efficiency of VMDP is a product of four contributing factors: Coupling efficiency between the input fiber and the optical waveguide (η_{FC}), carrier transit time frequency response ($\eta_{TR}(f)$), RC time constant limitation of the individual photodiode ($\eta_{RC}(f)$), and

102

the VMDP structure itself ($\eta_{VMDP}(f)$, including the minimized velocity mismatch, loss of the microwave transmission line, and the coupling loss of the wave function between passive and active waveguide regions). The overall efficiency can be expressed as:

$$\eta_{ALL}(f) = \eta_{FC} \cdot \eta_{TR}(f) \cdot \eta_{RC}(f) \cdot \eta_{VMDP}(f) \tag{17}$$

The combined effect of the RC limit of individual photodiode and the VMDP structure has been shown in Sec. IV.1. The transit time frequency response has been studied by Lucovsky et al. [22]. For the MSM photodiodes in VMDP, the finger spacing is 0.2 μm. Assuming the saturation velocities for holes and electrons are $V_p = 0.6 \times 10^7$ cm/sec and $V_n = 0.8 \times 10^7$ cm/sec, respectively, the 3-dB bandwidth for the transit time frequency response is ~ 250 GHz, as shown in Fig. 9.

A lensed fiber is employed to couple light from the optical fiber to the optical waveguide of the VMDP. It is made using the Ericsson Fusion Splicer FSU 925 and has a diameter of 18 μm. The coupling efficiency Γ can be calculated using the theory in [23-26]. A maximum coupling efficiency of 48% can be achieved with proper alignment. The alignment tolerance is also simulated. Within ±6 μm misalignment for the direction perpendicular to epitaxial layer junction and ±2.7 μm misalignment for the lateral direction, the coupling efficiency remains greater than 50% of the maximum value.

The simulation results for the frequency responses of VMDP with various number of photodiodes are shown in Fig. 10. The length of each MSM photodiode is 15 μm, and the spacing between active photodiodes is 150 μm. The coupling efficiency from the lensed fiber is not taken into account in this simulation since it varies with different lensed fiber tip design. The bandwidth of the VMDP with one MSM photodiode is basically the same as that of the conventional high speed MSM photodetector [6], and can be as high as several hundred GHz, though the quantum efficiency is low because of the high power design. The quantum efficiency increases with increasing number of photodiodes, with very slight decrease in the bandwidth, as shown in Fig. 11. A bandwidth-efficiency product over 80 GHz can be achieved if the number of photodiodes is greater than eight. The maximum quantum efficiency of 40% is limited by the 50 Ω-matched input termination assumption (50% of photocurrent propagates in the opposite direction of the light and is absorbed by the terminated input end) and the coupling loss between the active and passive waveguide regions (theoretical coupling efficiency = 98%). The quantum efficiency of VMDP can be doubled by employing open-circuit input termination, however, at the expense of detector bandwidth since the microwave reflected from the input end is not in phase with the forward traveling wave.
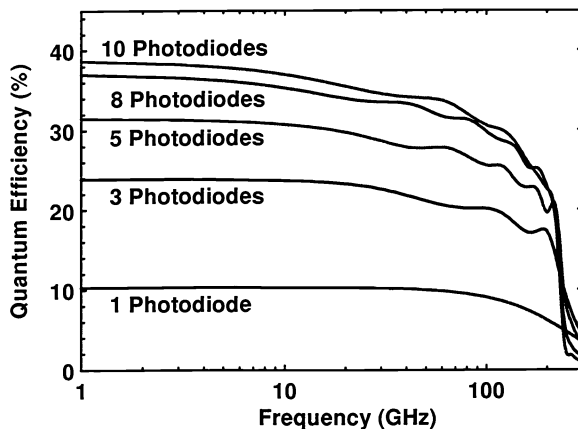
Fig. 10 Frequency responses of VMDP with various number of photodiodes.
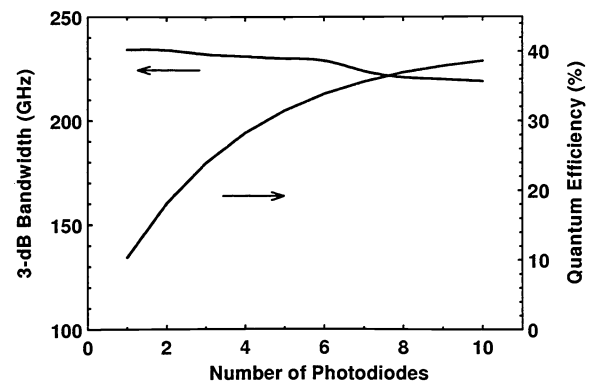
Fig. 11 3-dB bandwidth and maximum quantum efficiency of VMDP versus number of photodiodes.

V. EXPERIMENTAL RESULTS

The schematic structure of the VMDP and the scanning electron micrograph (SEM) of the MSM pattern is shown in Fig. 12. As mentioned previously, nanoscale MSM photodiodes are chosen as the active photodiodes because of their low parasitics and the ease of integration with the microwave transmission lines. However, it should be noted that the VMDP concept can be applied to other photodiodes such as p-i-n. The fabrication process of the MSM VMDP has been reported in [15]. In this section, the experimental results of the VMDP will be demonstrated.

The DC quantum efficiency of the VMDP is measured using a femtosecond tunable Ti:Sapphire laser as the light source. The laser is not modelocked for the DC measurement. The wavelength of the laser is tuned to 860 nm. Figure 13 shows the DC photocurrent versus the input optical power for the VMDP. Linear relationship is observed throughout the measurement range. The external quantum efficiency is equal to 12.3% (electron/photon) for uncoated facet. The quantum efficiency of the device can be improved by optimizing the coupling efficiency of the lensed fiber (currently ~ 48%) and applying anti-reflection (AR)-coating to the VMDP facet (30% Fresnel loss), as well as improving the coupling efficiency between the passive and active waveguide regions by better controlling the etching steps in the fabrication.
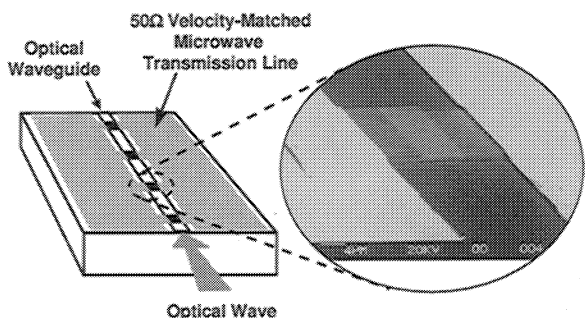
Fig. 12   Schematic structure of the VMDP and the scanning electron micrograph (SEM) of the MSM patterns.
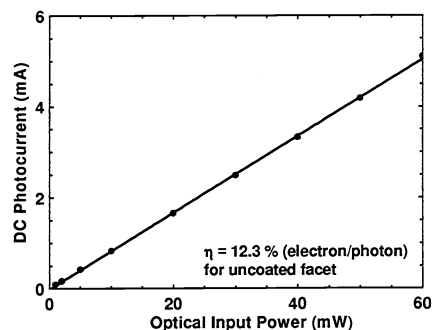
Fig. 13   DC photocurrent versus the optical input power for VMDP. The device is not saturated throughout the measurement range.

For the frequency response and saturation photocurrent measurement, the femtosecond Ti:Sapphire laser is modelocked at 860 nm with a pulse width of 120 fs and a repetition rate of 80 MHz. The light is focused into a 3-dB fiber coupler. The output from one branch is measured by an optical power meter for power monitoring. The other output is focused into the device using the lensed fiber. The device under test was biased at 4V through a bias-Tee. The generated microwave signal was collected at the output end of the transmission line by a 50 GHz high frequency probe (Picoprobe from GGB Industries). The signal is then sent to an HP digitizing oscilloscope with 50 GHz bandwidth through a microwave cable. Part of the signal is split by a microwave power splitter and amplified to trigger the digitizing oscilloscope. The timing jitters of the measured signal are greatly reduced in this configuration.

The electrical frequency response is obtained from the Fourier transform of the impulse response, as shown in Fig. 14. The input end of the transmission line on the device is not terminated in this measurement. The ringing in the trailing edge results from the microwave amplifier for the triggering signal. The frequency response of the microwave cable, splitter, amplifier, bias-T, and probe is separately characterized up to 50 GHz by HP 8510C network analyzer. The 3-dB bandwidth of 49 GHz for the calibrated response appears to be limited by the bandwidth of the digitizing oscilloscope.

To investigate the AC saturation effect, the impulse response of the VMDP is measured with increasing optical powers. The result is shown in Fig. 15. The pulse width increases slightly and a long tail in the trailing edge starts to develop in the impulse response under intense illumination. The

104

degradation in the speed of the photodetector is attributed to the electric field screening effect due to the large amount of photo-generated carriers. The saturation point is defined at 1-dB compression of the AC quantum efficiency, normalized to DC quantum efficiency. The peak photocurrent obtained by dividing the peak voltage of the impulse response with the 50 Ω load at 1-dB compression is equal to 56 mA [15]. The 3-dB bandwidths under different illumination intensity for the VMDP are also calculated using Fourier transform on the impulse response. The results are shown in Fig. 16. The bandwidth remains unchanged as the peak photocurrent increases to 19 mA (η_{AC}/η_{DC} ~ 0 dB), and reduces to 42 GHz when η_{AC}/η_{DC} decreases to -1 dB.
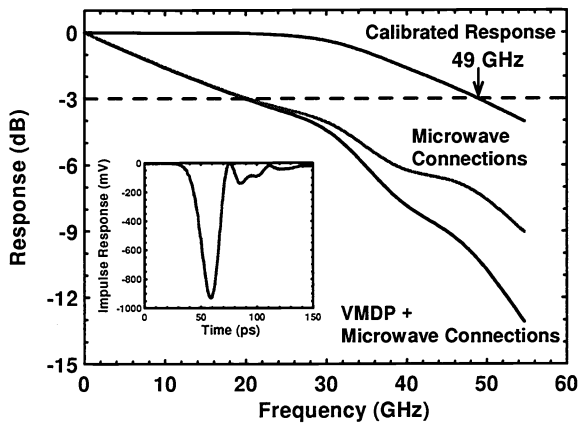
Fig. 14 The impulse response (inset) and the frequency response obtained from Fourier transform of the impulse of the VMDP.
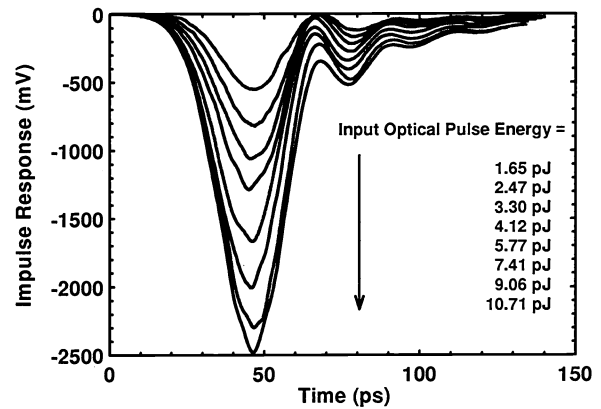
Fig. 15 Impulse response of the VMDP under various illumination intensity.
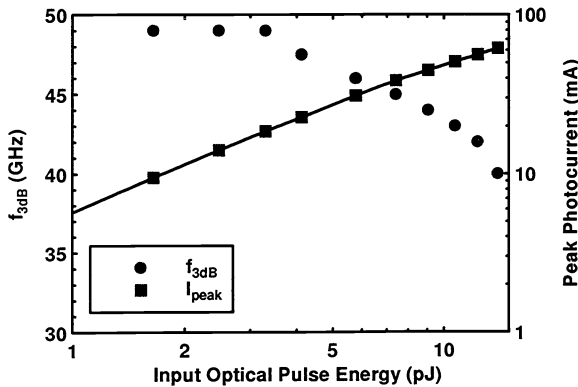
Fig. 16 The 3-dB bandwidth and the peak photocurrent versus the input optical pulse energy for VMDP.
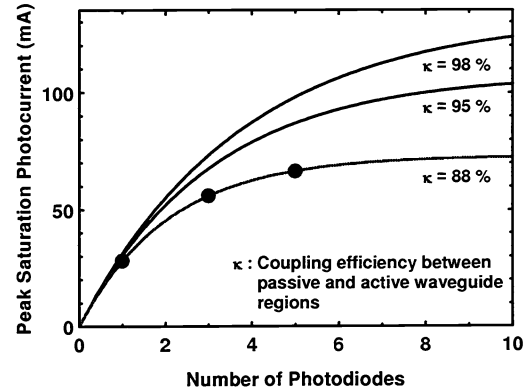
Fig. 17 The theoretical and experimental saturation peak photocurrents of VMDP versus the number of photodiodes for three coupling efficiencies

The saturation photocurrent is also measured for VMDP with 1 and 5 photodiodes. The results are shown in Fig. 17. The bandwidth of the VMDP with 3 photodiodes is the same as that of the VMDP with 1 photodiode, and degrades slightly when the number of the photodiodes increases to 5. Also shown in Fig. 17 are the calculated saturation peak photocurrent versus the number of photodiodes for different coupling efficiencies between the passive and active waveguide regions. The measured data agrees well with the curve of κ = 88%. This coupling efficiency is somewhat lower than the theoretical value of 98%. The discrepancy is attributed to the slight overetch during removal of the absorbing layer. By employing

selective etching, better coupling efficiency is expected. The saturation peak photocurrent can be further increased to > 100 mA by improving the coupling efficiency from 88% to 95% and increasing the number of photodiodes to ten.

The impedance and phase velocity of the periodically loaded transmission line on VMDP is characterized from 0.13 GHz to 50 GHz using HP 8510C network analyzer. Two-port measurement for transmission lines was employed. The impedance of the transmission line is obtained from the Smith chart, as shown in Fig. 18. The transmission line has an impedance close to 50 Ω (within 6 % deviation) throughout the measurement range. For the phase velocity measurement, time delay of the microwave signal between the two calibration planes (two probe tips) is characterized. From the length of the transmission line between the two calibration planes, the microwave phase velocity can be determined. The result is shown in Fig. 19. The theoretically simulated phase velocity (see Fig. 2) is superimposed on the experimental curve. Reasonably good agreement is obtained.
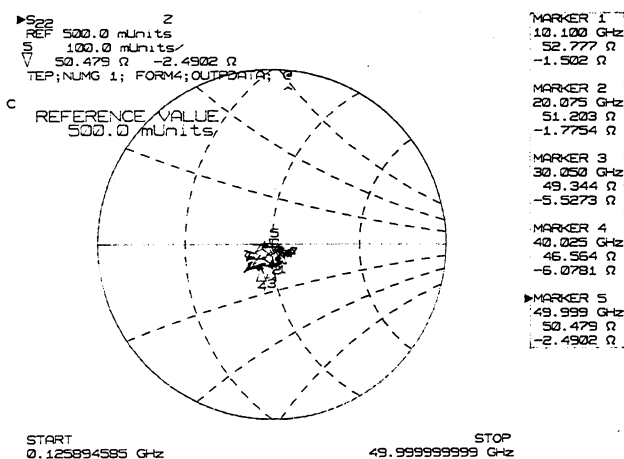
Fig. 18 Smith chart generated by the HP 8510C network analyzer for the impedance measurement of VMDP.
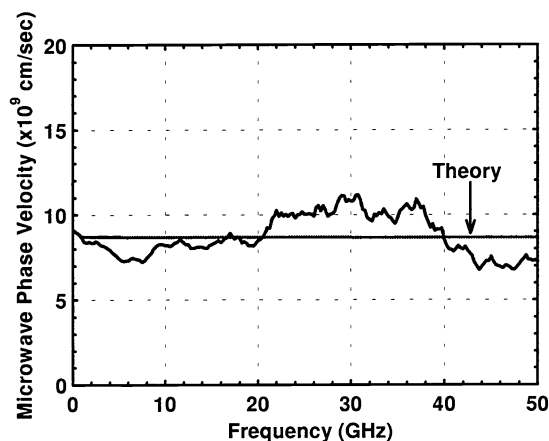
Fig. 19 The experimental and theoretical phase velocity of the periodically loaded transmission line on the VMDP.

VI. CONCLUSION

We have proposed the velocity-matched distributed photodetector (VMDP) to achieve high saturation power and large bandwidth. The theoretical analysis on the trade-off between saturation power and bandwidth shows that VMDP provides fundamental advantages over conventional photodetectors. Theoretical models have been developed to design and simulate the performance of VMDP. The VMDPs with nanoscale metal-semiconductor-metal (MSM) photodiodes have also been experimentally demonstrated. A very high saturation photocurrent of 56 mA and an instrument-limited 3-dB bandwidth of 49 GHz have been achieved. Further improvement in optical saturation power and quantum efficiency is expected with more precise control of the fabrication processes. The external quantum efficiency can also be improved by increasing the coupling efficiency from the lensed fiber and applying AR-coating on the input facet of the optical waveguide. The theoretical analysis and the experimental results show that VMDP can greatly improve the RF insertion loss, dynamic range, and noise performance of analog fiber-optic links. It is also attractive for high-power optical-microwave applications and optoelectronic generation of high power microwaves and millimeter-waves.

106

References:

[1] C. H. Cox, "Analog fiber-optic links with intrinsic gain," *Microwave Journal*, Vol. 35, no. 9, p. 92-99, 1992.

[2] C. H. Cox, "Gain and noise figure in analogue fibre-optic links," *IEE Proc.-J*, Vol. 139, no. 4, p. 238-242, 1992.

[3] R. F. Kalman, J. C. Fan, and L. G. Kazovsky, "Dynamic range of coherent analog fiber-optic links," *J. Lightwave Tech.*, Vol. 12, no. 7, p. 1263-1277, 1994.

[4] Y. G. Wey, K. Giboney, J. Bowers, M. Rodwell, P. Silvestre, P. Thiagarajan, and G. Robinson, "110-GHz GaInAs/InP double heterostructure p-i-n photodetectors," *J. Lightwave Tech.*, Vol. 13, no. 7, p. 1490-1499, 1995.

[5] K. D. Li, A. S. Hou, E. Ozbay, B. A. Auld, and D. M. Bloom, "2-picosecond, GaAs photodiode optoelectronic circuit for optical correlations," *Appl. Phys. Lett.*, Vol. 61, no. 26, p. 3104-3106, 1992.

[6] S. Y. Chou and M. Y. Liu, "Nanoscale tera-hertz metal-semiconductor-metal photodetectors," *IEEE J. Quantum Elec.*, Vol. 28, no. 10, p. 2358-2368, 1992.

[7] K. Kato, A. Kozen, Y. Muramoto, Y. Itaya, T. Nagatsuma, and M. Yaita, "110-GHz, 50%-efficiency mushroom-mesa waveguide p-i-n photodiode for a 1.55-μm wavelength," *IEEE Photonics Tech. Lett.*, Vol. 6, no. 6, p. 719-721, 1994.

[8] K. S. Giboney, R. L. Nagarajan, T. E. Reynolds, S. T. Allen, R. P. Mirin, M. J. W. Rodwell, and J. E. Bowers, "Travelling-wave photodetectors with 172-GHz bandwidth and 76-GHz bandwidth-efficiency product," *IEEE Photonics Tech. Lett.*, Vol. 7, no. 4, p. 412-414, 1995.

[9] A. R. Williams, A. L. Kellner, and P. K. L. Yu, "Dynamic range performance of a high speed, high saturation InGaAs/InP pin waveguide photodetector," *Elec. Lett.*, Vol. 31, no. 7, p. 548-549, 1995.

[10] H. F. Taylor, O. Eknoyan, C. S. Park, K. N. Choi, and K. Chang, "Traveling wave photodetectors," in *SPIE: Optoelectronic Signal Processing for Phased-Array Antennas II*, Vol. 1217, p. 59-63, 1990.

[11] V. M. Hietala, G. A. Vawter, T. M. Brennan, and B. E. Hammons, "Traveling-wave photodetectors for high-power, large-bandwidth applications," *IEEE Trans. On Microwave Theory and Tech.*, Vol. 43, no. 9, p. 2291-2298, 1995.

[12] R. E. Collin, *Foundations for Microwave Engineering*, 2nd ed., Ch. 8, 1992.

[13] M. C. Wu and T. Itoh, "Ultrafast photonic-to-microwave transformer (PMT)," in *IEEE LEOS Summer Topical Meeting on Optical Microwave Interactions*, Santa Barbara, CA, July 19-21, 1993.

[14] L. Y. Lin and M. C. Wu, "Ultrafast high power photodetectors," in *IEEE LEOS Summer Topical Meetings*, Keystone, CO, Aug. 7-11, 1995.

[15] L. Y. Lin, M. C. Wu, T. Itoh, T. A. Vang, R. E. Muller, D. L. Sivco, and A. Y. Cho, "Velocity-matched distributed photodetectors with high-saturation power and large bandwidth," *IEEE Photonics Tech. Lett.*, Vol. 8, no. 10, p. 1376-1378, 1996.

[16] K. J. Williams, R. D. Esman, and M. Dagenais, "Nonlinearities in p-i-n microwave photodetectors," *J. Lightwave Tech.*, Vol. 14, no. 1, p. 84-96, 1996.

[17] J. E. Bowers and C. A. Burrus, "Ultrawide-band long-wavelength p-i-n photodetectors," *J. Lightwave Tech.*, Vol. 5, no. 10, p. 1339-1350, 1987.

[18] L. Y. Lin, Ph.D. Dissertation, UCLA, 1996.

[19] K. C. Gupta, R. Garg, and I. J. Bahl, *Microstrip Lines and Slotlines*, Ch. 7, Artech House, 1979.

[20] G. Hasnain, A. Dienes, and J. R. Whinnery, "Dispersion of picosecond pulses in coplanar transmission lines," *IEEE Trans. Microwave Theory Tech.*, Vol. 34, no. 6, p. 738-741, 1989.

[21] H. Kogelink, *"Theory of Optical Waveguides"*, in *Guided-Wave Optoelectronics*, T. Tamir, Ed., Springer-Verlag, 1988.

[22] G. Lucovsky, R. F. Schwarz, and R. B. Emmons, "Transit-time considerations in p-i-n diodes," *J. Appl. Phys.*, Vol. 35, no. 3, p. 622-628, 1964.

[23] B. Hillerich, "Shape analysis and coupling loss of microlenses on single-mode fiber tips," *Appl. Opt.*, Vol. 27, no. 15, p. 3102-3106, 1988.

[24] D. Marcuse, *Light Transmission Optics*, 2nd ed., New York: Von Nostrand Renhold, 1982.

[25] D. Marcuse, "Loss analysis of single-mode fiber splices," *Bell Syst. Tech. J.*, Vol. 56, no. 5, p. 703-718, 1977.

[26] A. Kotsas, H. Ghafouri-Shiraz, and T. S. M. Maclean, "Microlens fabrication on single-mode fibers for efficient coupling from laser diodes," *Opt. and Quantum Elec.*, Vol. 23, p. 367-378, 1991.